# Optimal control of a nitrogen-vacancy spin ensemble in diamond for sensing in the pulsed domain

Andreas F. L. Poulsen,[1,*] Joshua D. Clement,[1,*] James L. Webb [1,†] Rasmus H. Jensen [1] Luca Troise,[1]
Kirstine Berg-Sørensen [2] Alexander Huck,[1,‡] and Ulrik Lund Andersen[1,§]

[1]*Center for Macroscopic Quantum States (bigQ), Department of Physics, Technical University of Denmark, 2800 Kongens Lyngby, Denmark*
[2]*Department of Health Technology, Technical University of Denmark, 2800 Kongens Lyngby, Denmark*

Defects in solid-state materials provide an ideal, robust platform for quantum sensing. To deliver maximum sensitivity, a large ensemble of noninteracting defects hosting quantum states with long coherence is required. Control of such an ensemble is challenging due to the spatial variation in both the defect energy levels and in any control field across a macroscopic sample. In this work, we experimentally demonstrate that we can overcome these challenges using Floquet theory and optimal control optimization methods to efficiently and coherently control a large defect ensemble, suitable for sensing. We apply our methods experimentally to a spin ensemble of up to $4 \times 10^9$ nitrogen-vacancy centers in diamond. By explicitly including the hyperfine interaction to the intrinsic $^{14}$N nuclear spin in the optimization, we design shaped microwave control pulses that can outperform conventional ($\pi$) pulses when applied to sensing schemes, with an improvement in the strength of ensemble response of between 11% and 78%. Through simulation of the ensemble dynamics, we shed light on the bandwidth limitations of large-ensemble reinitialization and propose alternative routes for further improvement.

## I. INTRODUCTION

Solid-state defects are a promising platform for quantum sensing, where purely quantum mechanical properties such as superposition and entanglement can be utilized to overcome classical limitations [1,2]. Particularly in semiconductors, where they can be controllably created and manipulated, solid-state defects can host quantum states that are both long lived and sensitive to the local environment in discrete energy levels within the band gap. A typical and extensively used defect system is the nitrogen-vacancy (NV) center in diamond. This consists of a substitutional nitrogen atom and an adjacent lattice vacancy, having discrete electronic and nuclear spin states with long coherence times up to room temperature [3]. The optical properties of the negatively charged NV center (NV$^-$) are highly sensitive to a range of parameters including magnetic field [4–9], electric field [5,10], temperature [11,12], and pressure (strain) [13]. Applications include sensing using a scanning diamond tip [14,15], nanoscale nuclear magnetic resonance (NMR)/electron spin resonance (ESR) [16,17], and in biophysics [18–21], where the robustness and high biocompatibility of diamond makes it an ideal platform for sensing, even within biological samples [22,23].

The level structure for a single NV$^-$ is illustrated schematically in Fig. 1(a), consisting of spin-triplet ground and excited states and metastable spin-singlet states [6,9,24–26]. When green laser light is absorbed by an NV in $m_s = 0$, red fluorescence is emitted from decay back into the triplet ground state. However, when absorbed in the spin split $m_s = \pm 1$, decay back to $m_s = 0$ may occur through singlet shelving states, via nonradiative and infrared emission at 1042 nm. The populations of $m_s = 0$ and $\pm 1$ can be controlled by applying resonant microwaves (at 2.87 GHz in the absence of an external bias magnetic field). This results in a detectable decrease in red fluorescence output on resonance, yielding a typical contrast $C$ of up to 30 % for a single NV [26] or $\sim 1\% - 2\%$ for a large ensemble with random orientation of NV centers (without preferential NV alignment through growth engineering [27]) and with intrinsic variability in local fields and material strain across the NV centers. The $m_s = \pm 1$ states can be split in energy, e.g., via the Zeeman effect by an external magnetic field, giving rise to multiple spectral features including additional subfeatures due to hyperfine splitting introduced by coupling to the nuclear spin of the $^{14}$N or $^{15}$N impurity atom [28]. By sweeping microwave frequency, these resonances can be identified by the drop in fluorescence output, a process termed optically detected magnetic resonance (ODMR) spectroscopy. By fixing the microwave drive frequency on or close to a resonance, any frequency shift resulting from the level shift of $m_s = \pm 1$ by magnetic field, electric field, or local temperature can be detected.

Sensing using NV centers can be performed by a simple continuous-wave (cw) method, maintaining a constant intensity of microwave and laser irradiation [25,29]. Alternatively, laser and microwave pulses can be used to control and read the ensemble [26,30]. This relies on the NV behaving as a two-level quantized system [31], with one (bright) maximally fluorescent state, $|0\rangle$, and one (dark) state with reduced

---

*These authors contributed equally to this work.
†Corresponding author: jaluwe@fysik.dtu.dk
‡alexander.huck@fysik.dtu.dk
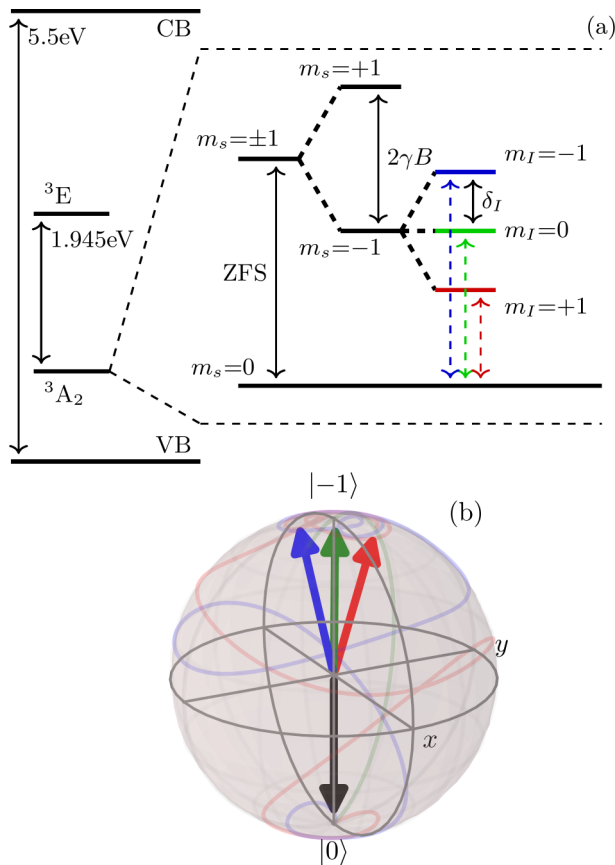§ulrik.andersen@fysik.dtu.dk

FIG. 1. (a) Simplified level diagram for a single $NV^-$ center within the diamond band gap, with the ground-state levels shown in detail. At zero magnetic field there is a splitting of 2.87 GHz [zero-field splitting (ZFS)] between the $m_s = 0$ and $m_s = \pm 1$ states. At finite field $B$, the Zeeman effect shifts the $m_s = \pm 1$ states in energy by $\gamma B$. The $m_s = \pm 1$ states are further split into three hyperfine levels ($m_I = 0, \pm 1$) separated by $\delta_I = 2.16$ MHz. (b) Bloch sphere representation depicting this $m_s = \{0, -1\}$ two-level system and the time evolution and result vector for a shaped optimal control microwave (MW) pulse applied to the initial $m_s = 0$ bright ground state ($|0\rangle$, black arrow). Here we show the time evolution into the $m_s = -1$ dark state for each of the hyperfine resonances $m_I$ ($|-1\rangle$, colored arrows).

fluorescence under illumination with green light, $|\pm 1\rangle$. For a single NV, these correspond to the electron spin states $m_s = 0$ and $\pm 1$, respectively. Rabi oscillations can be observed in $C$ on application of a microwave field resonant with the ground-state splitting. This system allows coherent control using discrete laser and microwave pulses, offering improvement over cw methods through reduction in the power broadening of the resonance linewidths. Techniques such as Ramsey interferometry [32,33] and Hahn echo-type sequences have been demonstrated [34,35], realizing single-molecule sensing in nanoscale diamond NMR experiments [36–38].

Pulsed schemes are used extensively for quantum sensing measurements using single- or few-NV centers, often in a confocal microscopy setup [39–41]. However, as extensive nuclear magnetic and electron spin resonance experiments

have shown, a macroscopic ensemble of many billions of electron or nuclear spins in a larger volume can also be manipulated by microwave pulse sequences in the same manner [42]. From a quantum sensing perspective, large ensembles are desirable for imaging applications [19], for vector sensing [43], or to maximize bulk sensitivity where spatial resolution is not required since the shot-noise-limited sensitivity scales as $1/\sqrt{N}$, with $N$ the number of defect centers [4]. However, ensemble NV sensing with flat (fixed amplitude and phase) microwave pulses suffers from nonuniform pulse operation. Inhomogeneous broadening due to strain and field gradients spreads the distribution of resonance frequencies of the NV centers, detuning many from the microwave drive frequency. These problems are further exacerbated by variation in near-field microwave drive frequency, power, and phase across the ensemble [44].

These effects have constrained state-of-the-art NV sensing to use of diamonds with a high degree of material optimization, including specialized high-energy (MeV-scale) irradiation [45], isotopic purification to reduce the diamond $^{13}$C content or to modify $^{15}$N content [46], strain engineering [47], preferential NV alignment via chemical vapor deposition (CVD) growth [27], and nanofabrication to increase fluorescence emission from the diamond [48]. However, it is not always possible to use such material optimization techniques. This can be due to limited accessibility to the necessary techniques and facilities, or can be due to application constraints, particularly for nanodiamonds, photonic devices including NV centers coupled to optical fiber [49,50], and portable microfabricated integrated devices [51]. In these applications, design limitations may impose constraints on the use of high-energy irradiation or leave high levels of mechanical strain or paramagnetic impurities [30] in the diamond.

An alternative approach is to manipulate the control fields (laser and microwave) to overcome nonuniform pulse operation. For higher-frequency AC sensing ($>10$ kHz), this includes techniques such as dynamical decoupling [7,35,52,53] and adiabatic chirped pulses [8]. However, these are not necessarily suitable for applications that require DC to low-frequency sensing, particularly for applications in biosensing [20,54–56]. An alternative in this frequency range is to deliver shaped microwave pulses (varying phase and amplitude), in order to boost fidelity in a Ramsey or pulsed ODMR [31] scheme. Such pulses can be designed using optimal control methods [34,57–59]. Optimal pulses have been used with small ensembles of NV centers for Hahn-echo [34,60] or Carr-Purcell sequences [61] to improve the robustness and temperature sensitivity of the D-Ramsey scheme [62], to extend the coherence time of an NV [63], and to improve the accuracy of entanglement operations [64].

In this work, we demonstrate the use of shaped microwave pulses produced by optimal control methods combined with Floquet theory that can deliver improved coherent control over a large solid-state defect ensemble of diamond NV centers. We show enhanced NV ensemble ODMR contrast an improved ensemble response to the environment, in terms of an applied test magnetic field, as compared to a conventional flat $\pi$-pulse scheme. Our scheme is widely adaptable to a range of solid-state systems where a two-level quantum system can be realized, although we specifically test our methods using

NV centers in diamond. We achieve our improvement through a full consideration of the physics of the system, including the hyperfine interaction with the nuclear spin of the substitutional nitrogen in the NV center (both $^{14}$N and $^{15}$N). We model ensemble behavior to further understand the physics of the system, in particular to explain the dynamics when a readout laser pulse is applied and to uncover new routes for improvement for sensing. We demonstrate our methods experimentally in off-the-shelf, standard grade material without significant processing or fabrication. Furthermore, we demonstrate operation at low Rabi frequencies, typical of those achievable using low-power microwave amplification, e.g., in a portable sensor device [65].

The paper is structured as follows. In Sec. II A we outline the basic methodology we use to construct and generate our shaped microwave pulses using optimal control theory, including our derivation for explicitly including the hyperfine interaction in the optimization algorithm. We describe a number of key control parameters, the limits of which we discuss in Sec. II B. In Sec. II C we describe in detail our experimental setup and methodology and in Secs. III A and III B we demonstrate the use of optimized shaped pulses for ODMR spectroscopy and detection of a test applied AC magnetic field. We compare using shaped pulses with a conventional $\pi$-pulse scheme using a flat microwave pulse, and analyze and discuss the optical behavior and how this relates to the physical dynamics of the NV ensemble.

## II. METHODS

### A. Optimal control

Our optimal control algorithm maximizes a functional that describes the desired transfer of one quantum state to another [25,34,58,59,66]. We define our state transfer functional as

$$\mathcal{F}_{\text{st}} = |\langle \psi_f | \hat{U}(t_p) | \psi_i \rangle|^2, \tag{1}$$

where $\mathcal{F}_{\text{st}}$ is the fidelity, of value between 0 and 1, which describes how well the pulse transfers the system from an initial state $|\psi_i\rangle$ to a final state $|\psi_f\rangle$. A fidelity of 1 represents a complete transfer to the desired state. The influence of the pulse is described by the unitary time-evolution operator $\hat{U}(t_p)$, where $t_p$ is the control pulse duration.

To represent the state transfer of a real ensemble, we calculate $\mathcal{F}_{\text{st}}$ for each member of a representative simulated ensemble of defects with a specified range of frequency detuning $\hat{\Delta}$ and relative control amplitude $\hat{\alpha}$. These factors are set to be representative of the variation across a real ensemble. The relative control amplitudes $\alpha_i$ represent the drive field inhomogeneity across the ensemble, and each value is the ratio between the Rabi frequency at which a given single defect is driven (due to drive field inhomogeneity) and the Rabi frequency at which the pulse is designed to drive the defects. The values of $\alpha_i$ thus vary around unity across the representative ensemble. The relative control amplitude only relates to the changes in Rabi frequency caused by drive field inhomogeneity and does not include the effects of frequency detuning on the Rabi frequency. The detuning is included in
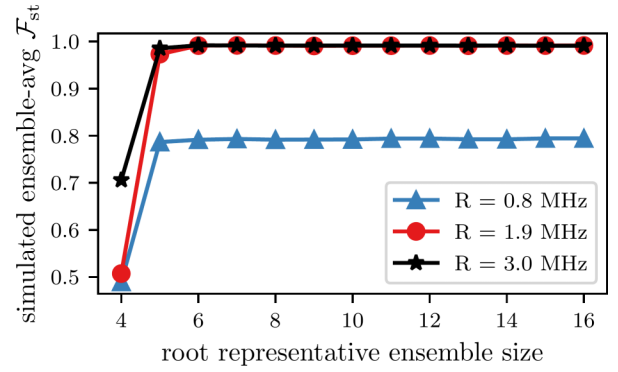


FIG. 2. The simulated weighted average fidelity of optimal control pulses $\mathcal{F}_{\text{st}}$ optimized with different ensemble sizes as a function of representative ensemble size for three values of the maximum allowed Rabi frequency $R_{\text{lim}}$. The pulses were optimized for $\hat{\Delta} = \pm 1$ MHz detuning, $\hat{\alpha} = 1 \pm 0.1$ amplitude variations, and a duration of $t_p = 1.85\ \mu$s with the indicated values of $R = R_{\text{lim}}$.

the optimization separately via the $\Delta_i$ values, which represent the inhomogeneous broadening. We thus assign each defect in the representative ensemble a value of $\alpha_i$ and $\Delta_i$ within the specified range $\hat{\Delta}$ and $\hat{\alpha}$ and seek a pulse that maximizes the average fidelity of the entire representative ensemble. Using this model assumes that interaction between defects is minimal, such that each defect can act as a single, isolated quantum system.

We assume our detunings $\Delta_i$ follow a Gaussian distribution centered at zero. The full width at half-maximum (FWHM) of this Gaussian distribution is set equal to half of the width of the considered detuning range $\hat{\Delta}$. The $\alpha_i$ values are assumed to follow a flat distribution over the considered range $\hat{\alpha}$. The weight of each defect in the representative ensemble is thus equal to the weight of its $\Delta_i$ value. These are normalized such that the sum of the weights of all defects in the representative ensemble is equal to 1. We therefore also use a weighted average of the fidelity. For numerical optimization, we use throughout this work a representative ensemble of size $12 \times 12$ (12 values to cover the ranges $\hat{\Delta}$ and $\hat{\alpha}$, respectively). This was based on a series of simulations of the performance of pulses transferring state $|0\rangle$ to $|-1\rangle$ [Fig. 1(b)] optimized using different representative ensembles. As shown in Fig. 2, $12 \times 12$ more than ensures convergence of the fidelity, while minimizing computational time.

For the design of our shaped microwave pulses, we use smooth optimal control. Here we choose a basis of periodic functions with the same periodicity $T$ and discretized frequency components, resulting in the shaped pulses becoming smooth in time [57]. In this work, we use a basis of sine functions with a fundamental frequency determined by the pulse duration $t_p$ [34]. Smooth optimal control has advantages over alternatives such as gradient ascent pulse engineering (GRAPE) [67] in that the bandwidth and the individual frequency components are known in advance, and the number of high-frequency components in the pulse Fourier spectrum is reduced, making modulation in experiments less technically demanding [57]. Our smooth optimal control pulse has the
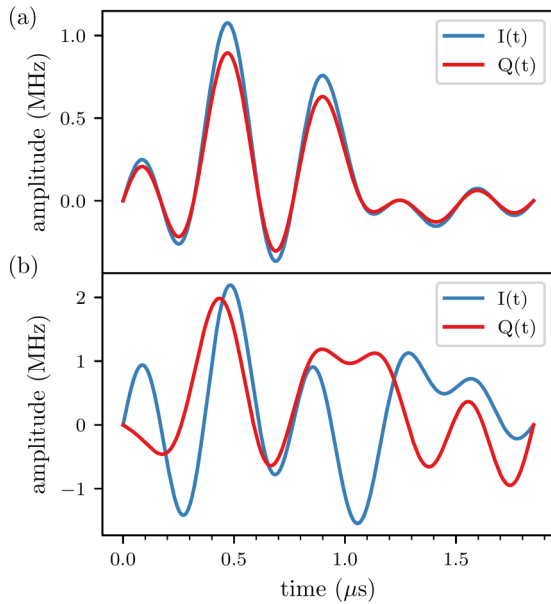
FIG. 3. Plot of $I(t)$ and $Q(t)$ in units of Rabi frequency for two optimal control pulses that were optimized by including state transfer using all three $^{14}$N hyperfine levels. The pulses were optimized for $\hat{\Delta}/2\pi = \pm 1$ MHz detuning and $\hat{\alpha} = 1 \pm 10\%$ amplitude variations with a duration of $t_p = 1.85$ $\mu$s and a maximum allowed Rabi frequency $R_{\lim}$ of (a) 1.4 MHz and (b) 3.0 MHz.

general form

$$S(t) = I(t)\cos(\omega_D t) + Q(t)\sin(\omega_D t), \qquad (2)$$

$$I(t) = \sum_{j=1}^{N_f} 2a_{jx}\sin(j\Omega_f t),$$

$$Q(t) = \sum_{j=1}^{N_f} 2a_{jy}\sin(j\Omega_f t). \qquad (3)$$

Here, $\omega_D$ is the central driving frequency, $\Omega_f = 2\pi/(2t_p)$ is the fundamental frequency, $N_f$ is the number of frequency components, and the real $a_{jk}$ values are control amplitudes. The bandwidth of such a pulse is then $N_f\Omega_f$. The fundamental frequency is not related to the Rabi frequency and purely serves to enforce the desired periodicity of $T = 2t_p$. The $a_{jk}$ values are defined in units of Rabi frequency $R$. As an example, Fig. 3 shows the in-phase and quadrature components $I(t)$ and $Q(t)$ used to modulate the microwave carrier for two of the specific pulses that we designed. In our experiments, the microwave carrier has a frequency $\omega_D/2\pi \approx 2.8$ GHz corresponding to the splitting between the $m_s = 0$ and $-1$ levels of the NV center $^3A_2$ ground state with an applied bias magnetic field.

It has been previously shown [60] that the performance of smooth optimal control pulses improves with increasing $N_f$ until it saturates for $N_f \geqslant 7$. We use $N_f = 10$ for all of our pulses to ensure that we are in the saturated regime. This yields 20 different control amplitudes $a_{jk}$ per shaped pulse, and these are the parameters that are optimized by the control algorithm. The optimization is carried out iteratively by stepping along the gradient of the fidelity with respect to the

control amplitudes with a step size $\beta$. Starting with initial control amplitudes $a_{jk}$, we compute the resulting $\hat{U}(t_p)$, $\mathcal{F}_{\text{st}}$, and $\frac{\partial \mathcal{F}_{\text{st}}}{\partial a_{jk}}$, before updating the control amplitudes by adding $\beta \frac{\partial \mathcal{F}_{\text{st}}}{\partial a_{jk}}$. This process is then repeated until $\mathcal{F}_{\text{st}}$ converges. The choice of time-periodic basis functions yields a time-periodic Hamiltonian that can be solved using Floquet theory [57,68,69].

In this work, we extend previous methods to include the effects of hyperfine splitting during the optimization. Although we specifically calculate for diamond NV centers here, this method is generally adaptable and applicable to any such splitting for a defect ensemble. The goal is to create a shaped pulse that performs the state transfer $|0\rangle$ to $|-1\rangle$ simultaneously and with as high fidelity as possible for each of the $m_l$ hyperfine levels. For an NV center ensemble, this results in a higher ODMR contrast than would be otherwise achievable by acting on only one $m_l$. This approach is analogous to continuous-wave methods driving multiple hyperfine lines previously described in the literature [70]. By doing this in the pulsed domain, we seek to achieve similar benefits, but without the negative effects of power broadening of the ODMR resonance linewidths. In order to explicitly account for the hyperfine splitting, it is necessary to modify the expression for the Fourier components of the Hamiltonian that make up the Floquet matrix. The Fourier components of the Hamiltonian are generally defined as

$$\hat{\mathcal{H}}_n = \frac{1}{T} \int_0^T \exp(-in\Omega_f t)\hat{\mathcal{H}}(t)\,dt, \qquad (4)$$

where $T = 2t_p$ is the periodicity of the Hamiltonian and $\hat{\mathcal{H}}(t)$ is the time-domain Hamiltonian that describes the system to be optimized. The nitrogen in an NV can be either $^{14}$N with $I = 1$ (highest natural abundance) or $^{15}$N with $I = \frac{1}{2}$, yielding either three or two hyperfine levels, respectively, as illustrated in Fig. 1(a). We assume hyperfine interaction between the $^{14}$N nuclear spins and the NV electron spins in the ensemble so that three hyperfine states are possible. The nuclear spins are assumed to be in a thermal state such that all $m_l$ hyperfine states are equally represented in the ensemble. The ODMR spectrum then contains three resonances separated by $\delta_l = 2.16$ MHz, corresponding to the three hyperfine resonances $m_l = -1, 0, 1$. We also assume that the different NV electron spins do not interact and that the $m_s = \pm 1$ states are clearly split by a static magnetic bias field. A single set of three NV centers that each correspond to one of the hyperfine transitions can then be reasonably approximated as three independent two-level systems. The drift Hamiltonian thus has the form

$$\hat{\mathcal{H}}_0 = \sum_{k=1}^{3} \frac{\omega_{0,k}}{2}\sigma_{z,k}, \qquad (5)$$

where $\hbar = 1$, $\omega_{0,k}$ is the transition frequency of hyperfine transition $k$, and $\sigma_{z,k}$ is a Pauli spin-$z$ matrix that is specific to transition $k$. Note that the above expression applies to any two-level defect with three equidistant hyperfine resonances that fulfills the underlying assumptions. The transition frequencies are related via $\omega_{0,1} = \omega_{0,2} - \delta_I$ and $\omega_{0,3} = \omega_{0,2} + \delta_I$. Given that the states of the three two-level systems can be completely described by a single vector of length 6, the $\sigma_{z,k}$ matrices can

also be represented by $6 \times 6$ matrices (see Appendix). The same is true of the $\sigma_{x,k}$ and $\sigma_{y,k}$ matrices. The control Hamiltonian describes the interaction between the control pulse of the form given in Eq. (2) and the three allowed transitions.

Assuming the control field is linearly polarized in the $x$ direction, which is perpendicular to the NV defect axis, the control Hamiltonian can be written in the form

$$\hat{\mathcal{H}}_c = \sum_{k=1}^{3} \sigma_{x,k}[I(t)\cos(\omega_D t) + Q(t)\sin(\omega_D t)], \qquad (6)$$

and the total Hamiltonian thus reads as

$$\hat{\mathcal{H}}(t) = \sum_{k=1}^{3} \left( \frac{\omega_{0,k}}{2}\sigma_{z,k} + \sigma_{x,k}[I(t)\cos(\omega_D t) + Q(t)\sin(\omega_D t)] \right). \qquad (7)$$

We can simplify the rest of the calculations by working in a rotating frame given by the unitary rotation operator

$$\hat{R} = \exp\left( \sum_{k=1}^{3} i\omega_D t\sigma_{z,k}/2 \right), \qquad (8)$$

which will commute with every term in $\hat{\mathcal{H}}_c$ except for $\sigma_{x,k}$. More precisely, $[\sigma_{z,k}, \sigma_{x,k'}] = 2i\sigma_{y,k}\delta_{k,k'}$ and $[\sigma_{z,k}, \sigma_{y,k'}] = -2i\sigma_{x,k}\delta_{k,k'}$.

The Baker-Campbell-Hausdorff lemma thus allows us to write

$$\hat{R}\hat{\mathcal{H}}_c\hat{R}^\dagger = \sum_{k=1}^{3} [\sigma_{x,k}\cos(\omega_D t) + \sigma_{y,k}\sin(\omega_D t)] \times [I(t)\cos(\omega_D t) + Q(t)\sin(\omega_D t)]. \qquad (9)$$

Using this expression and defining the detuning $\Delta = \omega_{0,2} - \omega_D$ as the difference between the transition frequency of the central hyperfine transition $\omega_{0,2}$ and the central driving frequency $\omega_D$, we obtain the expression

$$\hat{\mathcal{H}}' = \sum_{k=1}^{3} \left( \frac{\Delta + w_k\delta_I}{2}\sigma_{z,k} + [\sigma_{x,k}\cos(\omega_D t) + \sigma_{y,k}\sin(\omega_D t)] \right. \left. \times [I(t)\cos(\omega_D t) + Q(t)\sin(\omega_D t)] \right), \qquad (10)$$

where $w_1 = -1$, $w_2 = 0$, and $w_3 = 1$. Expanding by using trigonometric relations, the above expression can be simplified by using the rotating-wave approximation to eliminate the fast-oscillating terms

$$\hat{\mathcal{H}}' = \sum_{k=1}^{3} \left( \frac{\Delta + w_k\delta_I}{2}\sigma_{z,k} + \frac{I(t)}{2}\sigma_{x,k} + \frac{Q(t)}{2}\sigma_{y,k} \right). \qquad (11)$$

Combining Eq. (11) with Eq. (3) and inserted into Eq. (4), the Fourier components of the Hamiltonian become

$$\hat{\mathcal{H}}_n = \sum_{k=1}^{3} \frac{1}{T} \int_0^T \exp(in\Omega_f t)\left( \frac{\Delta + w_k\delta_I}{2}\sigma_{z,k} \right. \left. + \sum_{j=1}^{N_f}[a_{jx}\sigma_{x,k} + a_{jy}\sigma_{y,k}]\sin(j\Omega_f t) \right) dt. \qquad (12)$$

The above expression can be further simplified by using the exponential form of a sine and the integral form of a Kronecker delta. Doing so yields the final expression for the Fourier components of the Hamiltonian when the effects of hyperfine splitting are taken into account

$$\hat{\mathcal{H}}_n = \sum_{k=1}^{3} \left( \frac{\Delta + w_k\delta_I}{2}\sigma_{z,k}\delta_{n,0} + \sum_{j=1}^{N_f} \frac{1}{2i}[a_{jx}\sigma_{x,k} \right. \left. + a_{jy}\sigma_{y,k}][\delta_{n,j} - \delta_{-n,j}] \right). \qquad (13)$$

We use Eq. (13) in the construction of the Floquet matrix for the computation of $\hat{U}(t_p)$ and $\frac{\partial \mathcal{F}_{st}}{\partial a_{jk}}$ as part of the update step of the optimal control algorithm. We include the corresponding derivation for two hyperfine levels ($^{15}$N for NV centers) in the Supplemental Material [71]. Control amplitude variations are included by multiplying the control amplitudes $a_{jx}$, $a_{jy}$ by the $\alpha_i$ value for the given defect in the representative ensemble.

In order to ensure the optimization of our control amplitudes converging while remaining within experimentally achievable limits, we include a penalty functional

$$\mathcal{F}_{pen} = -pt_p \sum_{j,k} a_{jk}^2 \qquad (14)$$

in our algorithm, applied at each update step. The penalty functional includes a specified penalty constant $p > 0$ and scales with the control amplitudes. We optimize using the gradient of the sum of the penalty functional and the state transfer fidelity $\mathcal{F}_{tot} = \mathcal{F}_{pen} + \mathcal{F}_{st}$. After each update step, the maximum amplitude of the optimal control pulse is computed in units of Rabi frequency, and if it exceeds the maximum allowed Rabi frequency $R_{lim}$, the penalty constant is increased by a step size $\Delta p$. If the maximum amplitude of the optimal control pulse does not exceed $R_{lim}$, the penalty constant is reduced by $\Delta p$. $R_{lim}$ is one of the inputs to the algorithm and is limited by the maximum achievable experimental Rabi frequency $R_{max}$. This method also prevents the algorithm remaining at local maxima compared to optimizing without a penalty functional.

As a demonstration of the effect of explicitly including all three hyperfine levels in the optimization, Fig. 4 shows a series of simulated fidelity maps for a single NV subject to a flat $\pi$ pulse and optimal control pulses with and without including the hyperfine components. The fidelity of a $|0\rangle$ to $|-1\rangle$ state transfer is directly proportional to the resulting ODMR contrast $C$ since the contrast will be maximal when all NV electron spins are in the $|-1\rangle$ state and minimal in the $|0\rangle$ state. All three pulses are in the regime $R_{lim} < \delta_l$. It is clear that the regular optimal control pulse has superior performance for a single hyperfine resonance. However, when considering the average of all three, the shaped pulse
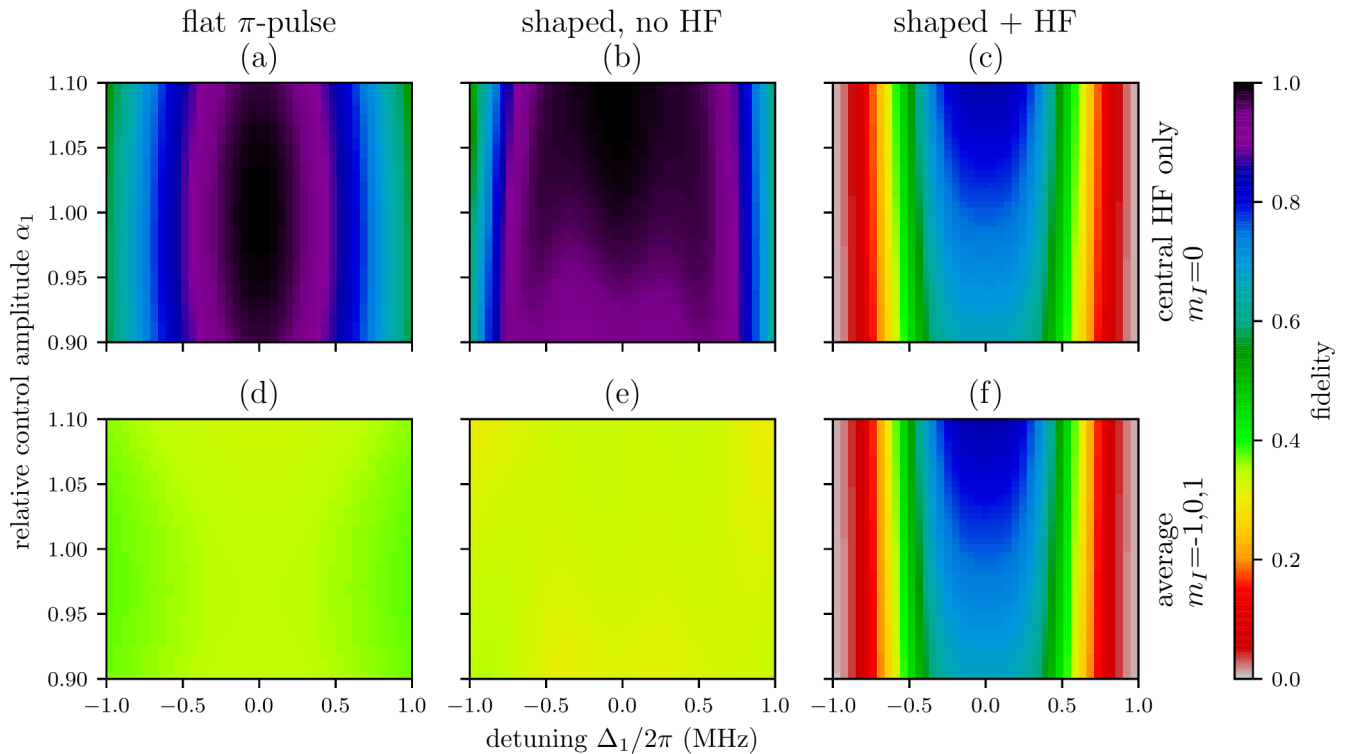
FIG. 4. Simulated maps of the state transfer fidelity [Eq. (1)] from $|0\rangle$ to $|1\rangle$ for a single NV ($i = 1$) subject to (a), (d) a flat ($\pi$) pulse, (b), (e) an optimized shaped pulse, and (c), (f) a shaped pulse optimized while taking all three hyperfine levels into account. The top plots (a)–(c) show the fidelity of the transfer experienced by the central hyperfine transition while the bottom plots (d)–(f) show the average of the transfer fidelities for each of the three hyperfine levels. Each point in the top plots is the fidelity for a single NV electron spin with the given values of $\alpha_1$ and $\Delta_1$. Each point in the bottom plots is the average of the fidelities for three NV electron spins with the given value of $\alpha_1$ and transition frequencies detuned by $\Delta_1$, $\Delta_1 + \delta_l$, and $\Delta_1 - \delta_l$, respectively, from the driving frequency. The flat pulse has a Rabi frequency of 1.4 MHz, and the optimal control pulses were both optimized using $\hat{\Delta} = \pm 1$ MHz detuning, $\hat{\alpha} = 1\% \pm 10\%$ amplitude variation, $R_{\text{lim}} = 1.4$ MHz, and a pulse duration $t_p = 1.85$ $\mu$s.

optimized while taking the effects of hyperfine splitting into account is significantly better, albeit within a narrower range of detuning. Figure 4(f) indicates that the optimal control pulse including the hyperfine splitting in the optimization is capable of simultaneously performing state transfer using all three hyperfine levels with high fidelity. The narrow range of high fidelity dropping rapidly with detuning indicates that the optimal pulse will yield high contrast when applied with drive frequency $\omega_D/2\pi$ close to any one of the three hyperfine resonances and low contrast when applied off resonance. This behavior naturally translates to higher contrast and narrow resonance linewidth and thus to a stronger ensemble response to the environment (higher sensitivity, with the same measurement noise floor). As can be seen in Figs. 4(c) and 4(f), as $\alpha_1$ is increased, the $|0\rangle$ to $|-1\rangle$ fidelity (i.e., ODMR contrast) further improves in the narrow range of high fidelity without significantly broadening the range of high fidelity. We therefore experimentally apply our optimal control pulses at applied microwave power equivalent to a higher maximum Rabi frequency than we use for optimization, empirically chosen to maximize the slope.

### B. Optimization details

All of our pulses were made using an initial value of the penalty constant $p = 1$ and $\Delta p = 0.05$. They were optimized

to perform a state transfer from $|0\rangle$ to $|-1\rangle$. We used 150 update steps for all of the optimizations, as this was found to be sufficient to achieve convergence of $\mathcal{F}_{\text{st}}$. For the first 51 steps, the step size along the gradient was kept constant at $\beta = 0.007$ and for the remaining steps, the optimal step size was determined using a line search. This was done to speed up the optimization without compromising the quality of the resulting optimal control pulses. We designed pulses using different values of $R_{\text{lim}}$, $t_p$, and the ranges $\hat{\Delta}$ and $\hat{\alpha}$ and tested them experimentally. We determined the maximum achievable experimental Rabi frequency, i.e., the upper limit on the maximum allowed Rabi frequency $R_{\text{lim}} \leqslant R_{\text{max}} = 3.2$ MHz through prior experimental measurements using flat pulses on the same diamond NV ensemble. Based on this, we defined a range of $R_{\text{lim}}$ to generate testable optimized shaped pulses for between $R_{\text{lim}} = 0.8$ MHz and $R_{\text{lim}} = 3.2$ MHz. The minimum value of $t_p$ necessary to achieve improvements over a comparable flat pulse was limited by the need to apply sufficient power to perform the desired state transfer. We set the lower limit of $t_p$ to be at least twice the duration of a flat $\pi$ pulse with Rabi frequency equal to $R_{\text{lim}}$. The maximum value of $t_p$ was ultimately by the $T_2$ coherence time of a single NV, but practically limited in this work to $t_p < 20$ $\mu$s by waveform generator technical constraints. Based on this, we defined a range of $t_p$ to generate testable optimized shaped pulses for s between $t_p = 1.0$ and $5.0$ $\mu$s.
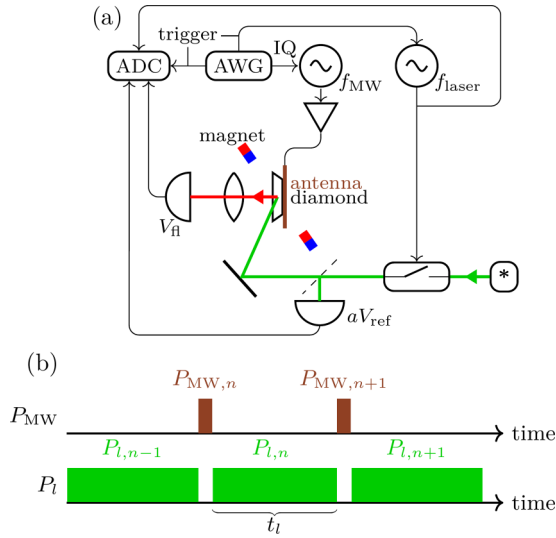
FIG. 5. (a) Schematic of our experimental setup. The pump laser was modulated by the AOM, at 2.6 MHz and controlled by the AWG. Microwave pulses were delivered to the diamond using a near-field antenna. The AWG provided IQ modulation to the signal generator to create the required control pulses. An ADC, synchronized with the AWG, digitized the analog AOM modulation signal, the signal from the APD collecting the diamond fluorescence $V_{fl}$ and the signal from an amplified photodetector that collects a small amount of the pump laser $V_{ref}$, balanced with $V_{fl}$. (b) Pulsed ODMR sequence as applied in our measurements, showing the repeating sequence of pump laser pulses $P_l$ and microwave pulses $P_{MW}$. This sequence was repeated continuously by the AWG.

Although the possible values of detuning $\Delta_i$ are in principle not limited, higher Rabi frequencies are required to compensate for higher levels of inhomogeneous broadening. Based on the considered values of $R_{lim}$, we therefore used $\hat{\Delta}$ up to $\pm 2$ MHz. The possible values of $\alpha_i$ are similarly not limited in principle, but higher Rabi frequencies are required to compensate for higher levels of drive field inhomogeneity. We therefore chose to optimize up to $\hat{\alpha} = 1 \pm 0.2$ relative control amplitude range.

Our initial $a_{jk}$ values were set using pseudorandom values within a range sufficient to yield a maximum Rabi frequency of the corresponding initial pulse $R > R_{lim}$. This was done in order to ensure that the optimization algorithm approached the region of allowed pulses from the outside, so that pulses utilizing $R_{lim}$ were considered. For this work, the initial Rabi frequency was 2.8 times greater than the maximum allowed Rabi frequency.

### C. Experimental setup

A schematic of our experimental setup is shown in Fig. 5(a). We used an off-the-shelf, general grade single crystal diamond (*SC Plate CVD, P2*, Element Six) with <1 ppm nitrogen impurities, ∼0.5 ppb NV⁻ concentration, of dimensions $6 \times 6 \times 1.2$ mm³. For this diamond, we measured a $T_2^*$-limited linewidth of 0.75 MHz. We measured best fit $T_1$ to be as 7.1 ms and $T_2$ and $T_2^*$ times of 387 and 0.44 $\mu$s, respectively, using Hahn-echo and Ramsey schemes, with a maximum ensemble-averaged Rabi frequency of $R_{max} =$

3.2 MHz driven by our antenna. In our Hahn-echo measurement we observe collapse and revival features arising from interaction with ¹³C spins [72]. Full details of these measurements are given in the Supplemental Material [71]. A bias field of 2.9 mT aligned along the [111] crystallographic axis was applied by fixed permanent magnets on electromechanical translation stages in order to split the $m_s = \pm 1$ states. We measured the field and optimized alignment using the ODMR recorded from the diamond and by using a gaussmeter to verify field amplitude. We addressed only the $m_s = 0 \rightarrow m_s = -1$ transition to use an effective two-level system within the antenna's resonance linewidth of ∼100 MHz.

The diamond was optically pumped using a 532 nm diode-pumped solid-state laser. For all work except Fig. 13 we used a Cobolt Samba 1500 capable of maximum 1.8-W output. For the data in the final figure, we used a lower power diode laser (Roithner Lasertechnik CW532-100F) of maximum output 100 mW. The linearly polarized laser beam was focused to a waist diameter of 120 $\mu$m and directed into the diamond at Brewster's angle to optically address (with at least $1/e^2$ the center intensity) an ensemble with a minimum estimated size of ≈$4 \times 10^9$ NV centers in a volume of ≈0.04 mm³ based on the focused waist of the pump beam. The maximum pump laser power we delivered to the diamond using the Cobolt laser was 500 mW (62 mW using CW532-100F). This resulted in a total of 84 $\mu$W (10.1 $\mu$W using CW532-100F) of red fluorescence escaping the front face of the diamond, of which we collected 0.91 $\mu$W (0.16 $\mu$W using CW532-100F) onto a small area avalanche photodiode (Thorlabs APD120A) using condenser lenses (Thorlabs ACL25416U) either side of a low-pass optical filter (FEL0550). Our APD operating in linear mode produced an amplified analog voltage output $V_{fl}$ sampled by an analog-to-digital converter (ADC, Gage Octopus CS8300) at 50 MSa/$sec$. We optically modulated our pump laser using an acousto-optic modulator (AOM, Isomet 532C-4) at $f_{AOM} = 2.6$ MHz, allowing us to perform software lock-in detection to minimize noise in the electronic readout. A fraction of the pump beam was also sampled by a second detector (Thorlabs PDA10A) to provide a reference, $V_{ref}$ for common-mode noise rejection.

We generated the microwave pulses necessary for implementation of the optimal control protocols using an arbitrary waveform generator (AWG, Tektronix 5000), in-phase/quadrature (IQ) modulating a Stanford SG394 RF signal generator. The microwave output was amplified (Mini-Circuits ZHL-16W-43-S+) and delivered to the diamond using a near-field antenna based on a square split-ring resonator design [73,74]. This antenna was designed for uniformity of near-field intensity in a $5 \times 5$ mm² region centered on the diamond with a resonance at approximately 2.8 GHz. Our AWG also controlled a switch (Minicircuits ZASWA − 2 − 50DRA+) through which the AOM modulation drive was passed, allowing the pump beam incident on the diamond to be pulsed and modulated.

### D. Pulse sequencing and readout

In our experimental setup, we measured contrast $C$, the change in fluorescence output as a result of a control pulse. We define $C$ as the change in fluorescence output in the

initial period of a pump laser readout pulse after application of a preceding microwave pulse [31,35,75]. $C$ was measured across an ODMR resonance feature by varying microwave drive frequency $\omega_D$. We measured this change in fluorescence signal $V_{fl}$ after application of either a shaped or flat microwave pulse, relative to the laser reference signal $V_{ref}$. We obtained $C$ by scaling the reference to the size of the fluorescence signal, subtracting the two, and integrating the resulting signal $V_{ref} - V_{fl}$ over a time window $t_w = 0.3$–$2.7$ ms at the start of the laser pulse (see Supplemental Material [71] for full details). This subtraction method allowed us to reject both DC and higher-frequency (>kHz) common-mode noise from the laser on the readout signal within the integration window. It also allowed us to measure a value for $C$ from every laser pulse, rather than measuring a reference with no microwave pulse on every other fluorescence readout, maximizing the bandwidth of our readout. From $C$ we also derived $C'$ the change in contrast with microwave drive frequency. This quantity, the slope of the ODMR resonance, gives a measure of the strength of ensemble response, in turn proportional to sensitivity to environmental factors such as magnetic field.

Using the pulsed protocol shown in Fig. 5(b), we first initialized the NV ensemble into the ground state using pump laser pulse $P_{l,n-1}$ of duration $t_l$. The pump laser was then blocked by the AOM during application of microwave control pulse $n$ of duration $t_p$. A subsequent laser pulse $P_{l,n}$ of the same duration $t_l$ was then applied and the state readout via NV fluorescence emission. This pulse also acted to reinitialize the system back into the $|0\rangle$ state, allowing the next $(n + 1)$ pulses to read and initialize. This method enabled measurements using only a short repeating sequence in the AWG memory. We acquired data continuously for repeated sequence sets up to the memory limit of the ADC ($n = 110$ pulses when using $t_l = 3$ ms). Once this limit was reached, the data were transferred to computer memory and processed, averaging over all pulse sequence sets in the acquisition to reduce noise, and then integrating to obtain $C$.

For direct comparison, we performed the same pulse sequence with the same readout methods for $C$ using both shaped microwave pulses and standard fixed amplitude and phase (flat) pulses. We also used the same method for calculating $C$ throughout our measurements, to ensure accurate comparison between the different microwave pulses. For flat pulses, we used pulses with a single microwave drive frequency of the form $\cos(\omega t)$ and three-frequency drive pulses of the form $\sum_{n\in\{0,\pm 1\}} \cos[(\omega + n\delta_l)t + \phi_n]$ to drive multiple $^{14}$N hyperfine transitions [70]. The latter were generated using the AWG with randomized phases $\phi_n$ for each ADC acquisition to eliminate time-dependent artifacts.

## III. RESULTS

### A. Laser pulse duration

Our previous measurements [24] demonstrated long optical reinitialization times, requiring many milliseconds on an approximately exponential decay with laser pulse duration to fully return the ensemble to the ground state. For the comparably sized ensemble in these experiments, we observed similar exponential behavior with a decay constant of of $\approx 1.4$ ms.
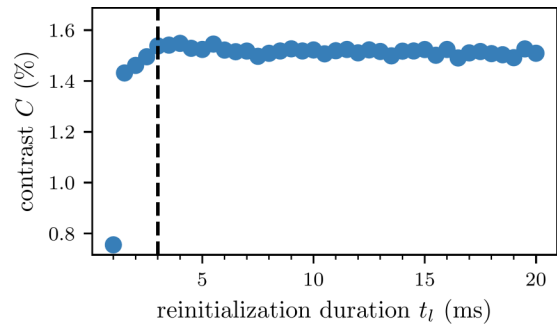


FIG. 6. Contrast as a function of laser pulse time $t_l$. Below 3 ms, $t_l$ is too short to sufficiently reinitialize the ensemble, leaving to a reduction in contrast $C$ with shorter readout/reinitialization laser pulse length $t_l$.

Waiting tens of milliseconds per readout would severely limit the number of pulses we could read and average in a single ADC acquisition and thus our contrast resolution and ultimately measurement bandwidth. We therefore first performed experiments varying laser pulse duration to determine whether we could initialize and control the ensemble using shorter laser pulses without suffering hysteresis effects, either from incomplete initialization or reionization delay across the readout laser pulses [76–78].

Figure 6 shows the contrast $C$ as a function of laser readout pulse duration $t_l < 20$ ms as measured using an optimal control pulse. We observed $C$ to be reduced for times shorter than $\approx 3$ ms, indicative that an increasing number of NV centers in the sample were not fully reinitialized into the ground state. For $t_l = 3$ ms and above, we observed negligible hysteresis effects in the fluorescence readout. This is supported by Fig. 7,
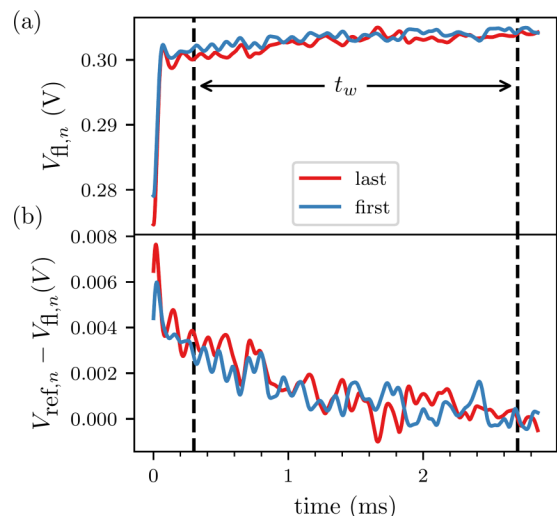


FIG. 7. Raw fluorescence readout signal $V_{fl,n}$ and relative contrast $C_{r,n}(t) = V_{fl,n} - V_{ref,n}$ for the first ($n = 1$) and last ($n = 110$) 3 ms readout laser pulse in a single ADC acquisition of 110 readout sequences. No difference within the readout noise was observed at this readout duration, as would be expected from hysteresis effects arising from insufficient reinitialization of the ensemble. Note that the artifact due to AOM switch-on is not included in the integration window $t_w$.
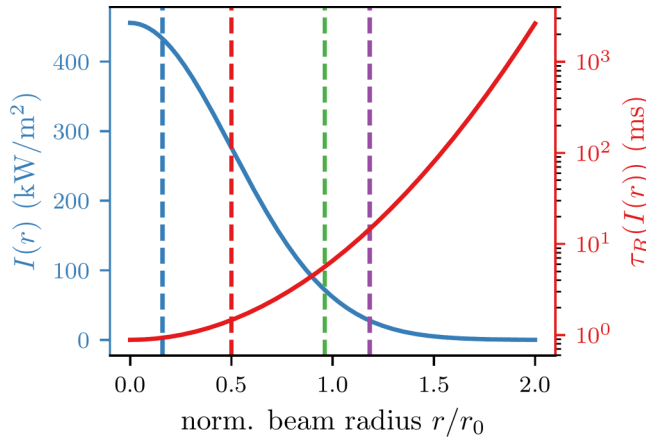
FIG. 8. Modeled variation in laser intensity $I(r)$ and the decay time $\tau_R[I(r)]$ of the reinitialization of the NV centers into the $m_s = 0$ ground-state level as a function of beam radius, relative to $r_0$ the $1/e^2$ beam width. The reinitialization time increases substantially at the lower intensity edges of the beam. The four dashed lines show the profile radii chosen to represent different regimes of beam intensity for hysteresis simulation in Fig. 9(a).

comparing the raw fluorescence readout and relative contrast calculated from the first and last individual readout pulses in a 110-pulse ADC acquisition using $t_l = 3$ ms.

We note that the fact we could achieve the same hysteresis-free contrast for a short 3-ms laser pulse as for one much longer is somewhat surprising. We consider that this effect primarily arises due to the Gaussian intensity profile of the laser, whereby the NV centers at the low-intensity edges of the beam require more time to reinitialize back into the ground state, but contribute far less to the overall fluorescence output, especially in the first few milliseconds of the readout laser pulse where contrast is measured [35]. In order to further investigate the physics of our NV ensemble and to determine the size of ensemble we address, we implemented a simple physical model of the NV population dynamics. Our model consists of a fixed NV density addressed by a radially (Gaussian) varying laser beam intensity, with an NV at radius $r$ from the beam center receiving a pump intensity $I(r)$. We then solve a rate model for all NV centers [79,80], from which we estimated the relative fluorescence output and ensemble contrast $C$. We model our microwave pulses as an ideal $\pi$ pulse with instantaneous population transfer in the rate model between levels $m_s = 0$ to $m_s = -1$. Further details of the implementation of the model are given in the Supplemental Material [71].

In Fig. 8, we plot the relative intensity $I(r)$ and the reinitialization time $\tau_R[I(r)]$, the exponential decay time required for the pump beam to return all NV centers at $r$ into the $m_s = 0$ ground state, as a function of beam radius $r/r_0$. Here $r_0$ represents the $1/e^2$ beam width as in our experiment. From this simulation, it is clear that the time period over which we integrate to derive the experimental contrast ($t_w = 0.3$–2.7 ms) corresponds to near complete reinitialization of the NV centers within $r/r_0 \approx 0.5$, or 25 % of the ensemble. Although this does not represent the entire ensemble, this still corresponds to $\approx 1 \times 10^9$ NV centers, based on estimated ensemble size
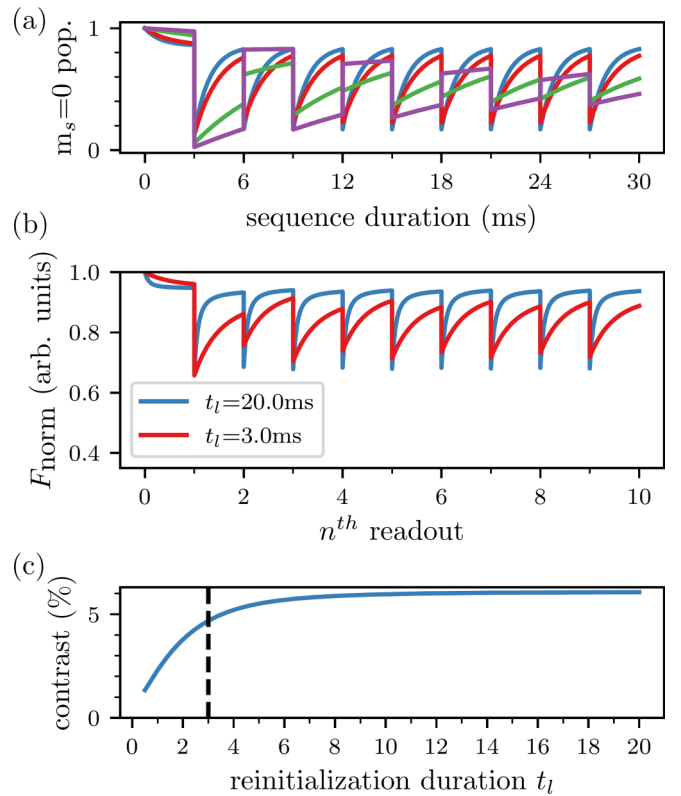


FIG. 9. (a) Simulated dynamics of the $m_s = 0$ population for NV centers receiving pump beam intensity $I(r)$ at four different increasing values of $r/r_0$ corresponding to Fig. 8. The simulation is initialized in $P(|0\rangle) = 1$ and evolved over 10 sequences of reinitialization and ideal $\pi$ pulses as in Fig. 5(b). (b) The ensemble-averaged $|0\rangle$ spin population from the simulation in (a), weighted by the radial distribution of fluorescence emission $I(r)r$. The hysteresis-free behavior of the defects within $r/r_0 < 0.5$ dominates the fluorescence output. The NV centers at the beam edge that are not fully reinitialized reduce the ensemble contrast as laser pulse length is reduced, as modeled in (c).

$(4 \times 10^9)$ from our experimental measurement of fluorescence emission.

The simulated reinitialization dynamic behavior can be seen in Fig. 9(a), plotting the time evolution of the $m_s = 0$ state population for the first 10 readout/MW pulses of length $t_l = 3$ ms for 4 increasing values of $r/r_0$. Below $r/r_0 = 0.5$, hysteresis-free behavior can be achieved in our model almost immediately after the first microwave pulse. Hysteretic behavior is observed for NV centers further towards the edge of the beam ($r/r_0 > 0.5$). For these NV centers, the ground-state occupancy decays to $\approx 50 \%$ within the first 10–20 pulses. These NV centers therefore contribute by a reduced amount to the contrast (as measured in $t_w$) as compared to the NV centers in the beam center ($r/r_0 < 0.5$), which exhibit the correct dynamics of full reinitialization by the laser and full state transfer by the microwave $\pi$ pulse. Since the outer NV centers are not fully reinitialized into the triplet ground state, they also act to produce a lower fluorescence emission as compared to the level expected with all NV centers reinitialized into the spin-triplet ground state. This can be seen in Fig. 9(b), showing the total ensemble fluorescence emission

as a function of time for $t_l = 20$ and 3 ms laser pulses. For the shorter pulse length, a greater number of NV centers are not fully reinitialized ($\tau_R < t_l$), reducing the overall fluorescence emission to approximately 90% of the maximum reached for $t_l = 20$ ms. Since the NV centers on the beam edge are not properly reinitialized into the ground state, they also cannot be correctly manipulated by the microwave state transfer pulse. As laser pulse length $t_l$ is reduced and this fraction of NV centers not fully reinitialized increases, this also contributes to a reduction in contrast $C$. This modeled behavior can be seen in Fig. 9(c) which qualitatively replicates our experimental data in Fig. 6.

The ability to rapidly read and reinitialize in this manner is an extremely useful result since it gives a means to adequately control and read a large NV ensemble with shorter laser pulses than that required to fully reinitialize every defect center. This significantly increases the measurement bandwidth for a pulsed sensing scheme, while still addressing a large number of defects.

### B. ODMR using shaped optimal control pulses

Using our optimal control algorithm including all three hyperfine levels for $^{14}$N, we first calculated a series of shaped microwave pulses spanning the parameter space of $\hat{\Delta}$ and $\hat{\alpha}$, the Rabi frequency limit $R_{\text{lim}}$, and the pulse duration $t_p$. Their performance was then tested experimentally to explore the limits of these parameters that yield high contrast $C$ and ODMR slope $C'$. We found that extending $\hat{\Delta}$ and $\hat{\alpha}$ beyond $\pm 1$ MHz and $\pm 10\%$, respectively, had negligible impact, likely indicating that the real ensemble distribution in our diamond was within these ranges. Having found that pulses in the range of $1.1$ MHz $< R_{\text{lim}} < 2.4$ MHz and $1\,\mu s < t_p < 2\,\mu s$ performed well, we experimentally searched the parameter space of these optimal control pulses applied by producing ODMR spectra using the shaped pulses and searching for the maximum slope $C'$. We also applied each optimal control pulse with experimental Rabi frequencies throughout the range $R_{\text{lim}} \leqslant R_{\text{expt}} \leqslant R_{\text{max}}$. We found the best-performing pulse optimized with $t_p = 1.85\,\mu s$ and $R_{\text{lim}} = 1.4$ MHz, with similar performance from larger $R_{\text{lim}}$ up to 2 MHz at the same $R_{\text{expt}}$. The modulation components $I(t)$ and $Q(t)$ for this pulse are shown in Fig. 3(a), and the control amplitudes are given in the Supplemental Material [71].

The experimental ODMR spectrum from the best shaped control pulse found is shown in Fig. 10(a). By differentiating the spectrum, we also show the frequency versus contrast slope $C'$ in Fig. 10(b). Here the largest possible slope is desired since this produces the maximum ensemble response. For comparison, we plot in the same figure the ODMR spectrum obtained using the best-performing conventional flat three-frequency drive ($\pi$) pulse. We found the maximum slope to be 11% higher for the shaped optimal control pulse than for this conventional flat pulse. Compared to the best-performing flat single-frequency drive ($\pi$) pulse, we measured a significant improvement of 73%. This corresponds directly to the same factor of improvement in sensitivity.

We note that the length of the flat and shaped pulse that delivered maximum slope were significantly different. This could potentially lead to the longer shaped pulse achieving
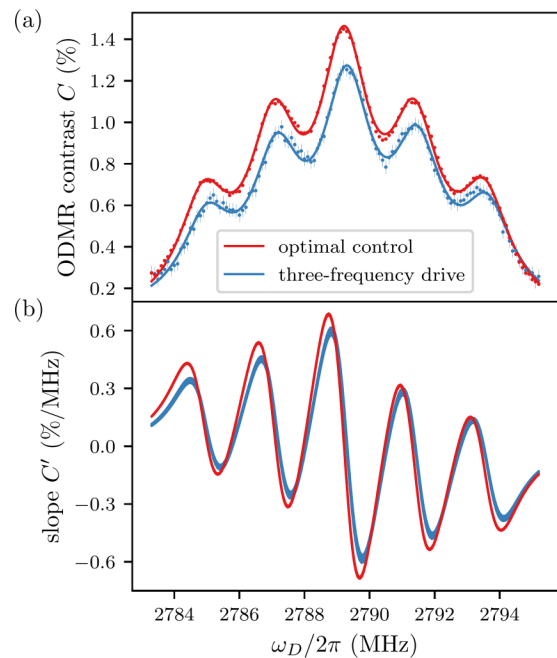


FIG. 10. Comparison of pulsed ODMR measurements using the best performing optimized shaped pulse and the flat pulse that delivers the highest contrast using three-frequency drive. The slope data shown in (b) are the slope of the fit to the ODMR data in (a).

higher performance purely by delivering more microwave power over an extended time period. To ensure this was not the case, we compared the optimized pulse against single- and three-frequency drive flat pulses over an extended parameter space of pulse lengths (up to $t_p = 1.35\,\mu s$) and applied microwave power (up to Rabi frequency $R_{\text{max}} = 3$ MHz). These data are shown in Fig. 11 for single-frequency drive and in Fig. 12 for three-frequency drive. The flat pulses performed best at the length and power that corresponded to performing a $\pi$ pulse on the largest possible subset of NV centers (maximizing contrast). However, as can be seen from these figures, the shaped microwave pulse we created using our optimal control methods always produced an ODMR slope far higher than any unshaped drive. This was the case for any pulse length or microwave power, with the optimum for the flat pulses reached well within experimental limits of $R_{\text{max}}$ and $t_p$.

To directly demonstrate the enhancement of NV center ensemble sensing response, we used a field coil aligned parallel to the static offset field to apply a test AC magnetic field to the diamond. We recorded the response in terms of the change in fluorescence emission (ODMR contrast) as a function of time, while using microwaves at central drive frequency $\omega_D$ corresponding to the point of maximum ODMR slope $C'$. We used the same experimental setup for both optimal and shaped pulses, with the same level of intrinsic noise. The results of these measurements for the best-performing shaped pulse as used for the ODMR plot in Fig. 11 and for a flat pulse can be seen in Fig. 13, the shaped pulse enhancing the response by $\approx 70\%$. This level of response was directly proportional to the enhancement of ODMR contrast and slope seen in Fig. 10. We verify this result further in the Supplemental Material
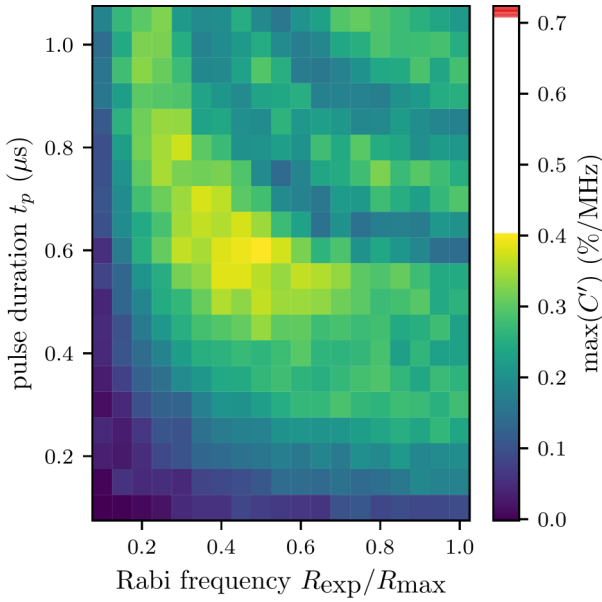
FIG. 11. The maximum ODMR slope $C'$ measured for flat single-frequency drive pulses over the relevant parameter space of applied Rabi frequency $R_{\text{expt}}$ and duration $t_p$. The red stripe in the color bar shows the maximum ODMR slope of the best optimal control pulse from Fig. 10. The equivalent plot for three-frequency drive is given in the Supplemental Material [71].

[71] through measurements of the amplitude spectrum of the response signal while varying coil current and AC frequency, including characterization of the readout noise and control measurements taken on and off microwave resonance.

## IV. CONCLUSION

In this work, we demonstrate that a large ensemble of solid-state defects in a macroscopic sample can be manipulated and coherently controlled in a manner beneficial for quantum sensing. We demonstrate this for an ensemble of NV centers in diamond through the use of shaped microwave pulses gen-
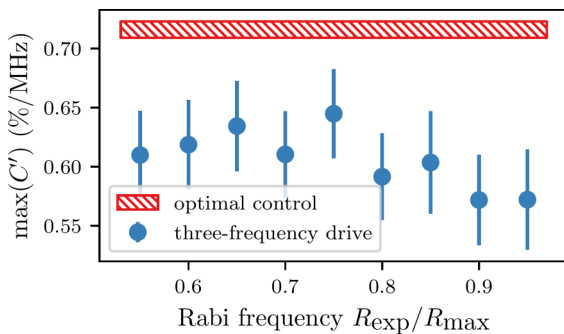


FIG. 12. Maximum ODMR slope $C'$ for three-frequency drive pulses of the best-performing duration $t_p$ for the given Rabi frequency $R_{\text{expt}}$, compared to the best-performing optimal control pulse. The error bars of the three-frequency drive data and the $y$ range of the optimal control pulse data represent $1\sigma$ uncertainty. The data covering the full parameter space in duration $t_p$ and Rabi frequency $R_{\text{expt}}$ are shown in the Supplemental Material [71].
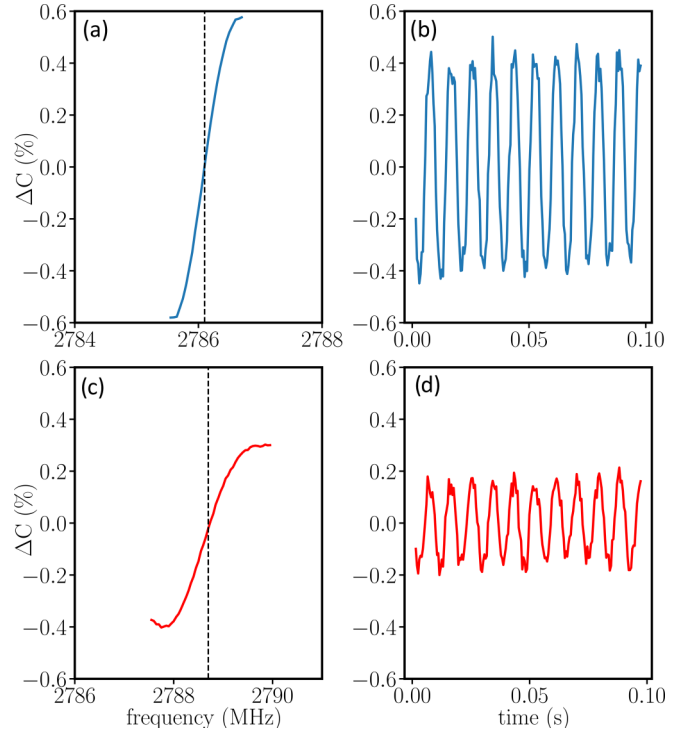


FIG. 13. (a) ODMR taken using an optimized shaped pulse, plotted as the change in $C$ with respect to the value at maximum slope $C'$ at $\omega_D = 2786.1$ MHz and (b) time series of the ensemble response when a 111-Hz AC magnetic field was applied to the diamond. The applied field was recorded as a clear signal in the fluorescence emitted by the NV centers. In (c) and (d) we show the equivalent ODMR and time response ($\omega_D = 2788.75$ MHz) measured using a flat MW pulse. We observed a clear increase in the ensemble response to the applied field using the shaped as compared to the flat pulse. The amplitude of the recovered signal was $\approx 70\%$ larger, directly proportional to the enhancement of ODMR slope $C'$ achieved by using the shaped pulse.

erated using Floquet theory and optimal control methods. Due to the scaling of sensitivity with the number of defects, such large ensembles are key for quantum sensing applications, either using NV centers or other solid-state defects. Both our overall NV ensemble volume within the estimated Gaussian beam width ($\approx 4 \times 10^9$ NV centers in a $\approx 0.04$ mm³ volume) and our estimated NV ensemble contributing maximally to the contrast signal ($\approx 25\%$ of the total) was larger than NV ensembles previously studied and reported in the literature using optimal control methods largely studied using confocal microscopy [34,57,60–63,81].

By fully considering the physics of the defect system and including the hyperfine interaction in our optimization, we demonstrate an 11 % enhancement in ODMR slope with optimized shaped pulses when compared to the best alternative three-frequency drive flat (fixed amplitude and phase) ($\pi$) pulses and a 78 % improvement over standard single-frequency-drive flat ($\pi$) pulses most commonly used for coherent control in the literature. This improvement is directly proportional to the same factor of sensitivity increase when used in an applied sensing scheme, as we demonstrate via sensing of an applied AC magnetic field. This significant

improvement offers potential for wider impact for DC and low-frequency sensing, for example, in precision measurement of slowly varying temperature where ensemble probe bandwidth limitations imposed by the $\approx 5$ $\mu$s shaped pulse length would be less constraining. Our method is not specific to the apparatus we used. By measuring the ODMR contrast by referring to the signal from an additional photodetector, we were able to reject more of the laser technical noise while maximizing the number of contrast measurements we could achieve as compared to alternative time-domain noise-rejection methods [35].

Through modeling of the physical dynamics of the readout and initialization of the defect ensemble, we show that although many tens of milliseconds are required to fully reinitialize the whole NV ensemble, a shorter laser pulse can address and reinitialize a large proportion of the NV centers. By demonstrating consistent contrast measurements free of hysteresis, we show that these NV centers can be addressed and controlled reliably. Further work is required to fully understand the dynamics of the system and the distribution of pump light in the diamond. However, our measurements suggest the primarily limiting factor on the readout is the Gaussian shape of the laser beam, hinting at considerable future improvement using a non-Gaussian profile.

The shaped microwave pulses we generate in this work almost certainly represent local maxima of performance in a wide parameter space. We consider it very likely that advances in methods for optimization as well as experimental improvements could provide even better solutions in the future. A particular disadvantage of our approach is the assumption of simple Gaussian distributions for detuning and other parameters, which are a poor representation of the actual properties of a real sample. A route forward may be to use experimental feedback in the optimization algorithm. This would be simplified by producing a more homogeneous microwave field through antenna improvements, increasing the ensemble Rabi frequency through better use of the microwave power, and the use of alternative laser beam profiles to improve uniformity of initialization and readout. Additionally, in this work we optimize for state transfer $|0\rangle$ to $|-1\rangle$, which aims to maximize contrast $C$. By instead explicitly optimizing for the change in contrast in response to the control field (the slope $C'$ in our results above), better optimized pulses could be generated. A further future approach would be to implement spin-bath driving [82] or use dynamic nuclear polarization [83] with shaped pulses that couple to longer-lived nuclear spins, including $^{13}$C [84], acting as an ancillary qubit to enhance sensing properties [32].

We consider our pulse shaping approach to be especially suitable to systems with a relatively large degree of inhomogeneous broadening and/or microwave drive variation. In particular, such a system arises in wide-field imaging of magnetic field using NV centers [85]. For a useful field of view of up to many tens of micrometers, suitable for biosensing or integrated circuit imaging, intrinsic factors within the diamond such as variation in strain and ODMR contrast along with extrinsic factors such as variation in pump laser power can produce a high degree of inhomogeneous broadening across NV centers in the imaged region. Furthermore, creating a

uniform power near-field microwave field across such a wide field of view is challenging, especially in the presence of variation in dielectric properties of the target system to be imaged. In this application, it is therefore extremely difficult for a single flat microwave pulse to correctly address all NV centers in the image, given a wide variation in Rabi and microwave drive frequency across the field of view. For a $\pi$ pulse or Ramsey sensing scheme, this then means highly nonuniform sensitivity and potentially even regions with zero sensitivity within the image.

The furthest extreme example of this type of wide-field imaging is sensing using a distribution of nanodiamonds across the imaging field of view. This configuration is highly suitable for NV temperature sensing, each diamond acting as a local probe of heat generation and flow, particularly from processes in biophysics [86]. It is extremely desirable to sense simultaneously from all such nanodiamonds, in order to monitor the interaction and operation of such processes. However, there exists extremely high variation in broadening between the few NV centers in each nanodiamond, which is induced by the geometry and high strain of the diamonds, plus potentially high variations in microwave drive, induced by variations in dielectric coupling due to local conditions (e.g., composition and density variation of of ionic solutions, such as intercellular or intracellular fluid). This far, existing implementations have had to rely on continuous-wave sensing, with sensitivity compromised by microwave power broadening of the ODMR resonances. For this application, pulse shaping offers the possibility to apply a single, shaped microwave pulse that is capable of interrogating NV centers across the field of view simultaneously, with higher sensitivity than cw and with image-wide high sensitivity and sensing bandwidth in a way a flat pulse cannot deliver.

Our work represents an important step in the direction of using optimal control and other techniques widely used in nuclear magnetic and electron spin resonance experiments to explore the physics of new systems suitable for quantum sensing. These techniques, including those we outline here, can be adapted to be widely applicable, not only to diamond but to other defects in both bulk and novel quantum materials, such as those in two-dimensional (2D) materials [87]. Using control pulses shaped by optimal control methods, which could be either microwaves, optical fields, or some other means, offers a good route to reach the ultimate $T_2^*$-limited performance, especially where extensive material optimization is not desirable or possible.

## APPENDIX: SPIN MATRICES

Following are shown the $6 \times 6$ matrix representations of the Pauli spin matrices that are each specific to one of the three nitrogen-14 hyperfine transitions:

$$\sigma_{z,1} = \begin{pmatrix} 1 & 0 & 0 & 0 & 0 & 0 \\ 0 & -1 & 0 & 0 & 0 & 0 \\ 0 & 0 & 0 & 0 & 0 & 0 \\ 0 & 0 & 0 & 0 & 0 & 0 \\ 0 & 0 & 0 & 0 & 0 & 0 \\ 0 & 0 & 0 & 0 & 0 & 0 \end{pmatrix}, \sigma_{z,2} = \begin{pmatrix} 0 & 0 & 0 & 0 & 0 & 0 \\ 0 & 0 & 0 & 0 & 0 & 0 \\ 0 & 0 & 1 & 0 & 0 & 0 \\ 0 & 0 & 0 & -1 & 0 & 0 \\ 0 & 0 & 0 & 0 & 0 & 0 \\ 0 & 0 & 0 & 0 & 0 & 0 \end{pmatrix}, \tag{A1}$$

$$\sigma_{z,3} = \begin{pmatrix} 0 & 0 & 0 & 0 & 0 & 0 \\ 0 & 0 & 0 & 0 & 0 & 0 \\ 0 & 0 & 0 & 0 & 0 & 0 \\ 0 & 0 & 0 & 0 & 0 & 0 \\ 0 & 0 & 0 & 0 & 1 & 0 \\ 0 & 0 & 0 & 0 & 0 & -1 \end{pmatrix}, \sigma_{x,1} = \begin{pmatrix} 0 & 1 & 0 & 0 & 0 & 0 \\ 1 & 0 & 0 & 0 & 0 & 0 \\ 0 & 0 & 0 & 0 & 0 & 0 \\ 0 & 0 & 0 & 0 & 0 & 0 \\ 0 & 0 & 0 & 0 & 0 & 0 \\ 0 & 0 & 0 & 0 & 0 & 0 \end{pmatrix}, \tag{A2}$$

$$\sigma_{x,2} = \begin{pmatrix} 0 & 0 & 0 & 0 & 0 & 0 \\ 0 & 0 & 0 & 0 & 0 & 0 \\ 0 & 0 & 0 & 1 & 0 & 0 \\ 0 & 0 & 1 & 0 & 0 & 0 \\ 0 & 0 & 0 & 0 & 0 & 0 \\ 0 & 0 & 0 & 0 & 0 & 0 \end{pmatrix}, \sigma_{x,3} = \begin{pmatrix} 0 & 0 & 0 & 0 & 0 & 0 \\ 0 & 0 & 0 & 0 & 0 & 0 \\ 0 & 0 & 0 & 0 & 0 & 0 \\ 0 & 0 & 0 & 0 & 0 & 0 \\ 0 & 0 & 0 & 0 & 0 & 1 \\ 0 & 0 & 0 & 0 & 1 & 0 \end{pmatrix}, \tag{A3}$$

$$\sigma_{y,1} = \begin{pmatrix} 0 & -i & 0 & 0 & 0 & 0 \\ i & 0 & 0 & 0 & 0 & 0 \\ 0 & 0 & 0 & 0 & 0 & 0 \\ 0 & 0 & 0 & 0 & 0 & 0 \\ 0 & 0 & 0 & 0 & 0 & 0 \\ 0 & 0 & 0 & 0 & 0 & 0 \end{pmatrix}, \sigma_{y,2} = \begin{pmatrix} 0 & 0 & 0 & 0 & 0 & 0 \\ 0 & 0 & 0 & 0 & 0 & 0 \\ 0 & 0 & 0 & -i & 0 & 0 \\ 0 & 0 & i & 0 & 0 & 0 \\ 0 & 0 & 0 & 0 & 0 & 0 \\ 0 & 0 & 0 & 0 & 0 & 0 \end{pmatrix}, \tag{A4}$$

$$\sigma_{y,3} = \begin{pmatrix} 0 & 0 & 0 & 0 & 0 & 0 \\ 0 & 0 & 0 & 0 & 0 & 0 \\ 0 & 0 & 0 & 0 & 0 & 0 \\ 0 & 0 & 0 & 0 & 0 & 0 \\ 0 & 0 & 0 & 0 & 0 & -i \\ 0 & 0 & 0 & 0 & i & 0 \end{pmatrix}. \tag{A5}$$

[1] T. Schröder, S. L. Mouradian, J. Zheng, M. E. Trusheim, M. Walsh, E. H. Chen, L. Li, I. Bayn, and D. Englund, Quantum nanophotonics in diamond [Invited], J. Opt. Soc. Am. B **33**, B65 (2016).

[2] I. Aharonovich, D. Englund, and M. Toth, Solid-state single-photon emitters, Nat. Photonics **10**, 631 (2016).

[3] J. H. N. Loubser and J. A. Van Wyk, Electron spin resonance in the study of diamond, Rep. Prog. Phys. **41**, 1201 (1978).

[4] J. M. Taylor, P. Cappellaro, L. Childress, L. Jiang, D. Budker, P. R. Hemmer, A. Yacoby, R. Walsworth, and M. D. Lukin, High-sensitivity diamond magnetometer with nanoscale resolution, Nat. Phys. **4**, 810 (2008).

[5] Z. H. Wang, G. de Lange, D. Risté, R. Hanson, and V. V. Dobrovitski, Comparison of dynamical decoupling protocols for a nitrogen-vacancy center in diamond, Phys. Rev. B **85**, 155204 (2012).

[6] D. Farfurnik, A. Jarmola, L. M. Pham, Z. H. Wang, V. V. Dobrovitski, R. L. Walsworth, D. Budker, and N. Bar-Gill, Improving the coherence properties of solid-state spin ensembles via optimized dynamical decoupling, in *Quantum Optics*, edited by J. Stuhler and A. J. Shields (SPIE, Bellingham, WA, 2016).

[7] D. Farfurnik, A. Jarmola, D. Budker, and N. Bar-Gill, Spin ensemble-based AC magnetometry using concatenated dynamical decoupling at low temperatures, J. Opt. **20**, 024008 (2018).

[8] G. T. Genov, Yachel Ben-Shalom, F. Jelezko, A. Retzker, and N. Bar-Gill, Efficient and robust signal sensing by sequences of adiabatic chirped pulses, Phys. Rev. Research **2**, 033216 (2020).

[9] F. Jelezko, T. Gaebel, I. Popa, A. Gruber, and J. Wrachtrup, Observation of Coherent Oscillations in a Single Electron Spin, Phys. Rev. Lett. **92**, 076401 (2004).

[10] F. Dolde, H. Fedder, M. W. Doherty, F. Rempp, G. Balasubramanian, F. Reinhard, F. Jelezko, and J. Wrachtrup, Sensing electric fields using single diamond spins, Nat. Phys. **7**, 459 (2011).

[11] P. Neumann, I. Jakobi, F. Dolde, C. Burk, R. Reuter, G. Waldherr, J. Honert, T. Wolf, A. Brunner, J. H. Shim, D. Suter, H. Sumiya, J. Isoya, and J. Wrachtrup, High-precision nanoscale temperature sensing using single defects in diamond, Nano Lett. **13**, 2738 (2013).

[12] T. Delord, L. Nicolas, M. Bodini, and G. Hétet, Diamonds levitating in a Paul trap under vacuum : Measurements of

laser-induced heating via NV center thermometry, Appl. Phys. Lett. **111**, 013101 (2017).

[13] M. W. Doherty, V. V. Struzhkin, D. A. Simpson, L. P. McGuinness, Y. Meng, A. Stacey, T. J. Karle, R. J. Hemley, N. B. Manson, L. C. L. Hollenberg, and S. Prawer, Electronic Properties and Metrology Applications of the Diamond nv⁻ Center Under Pressure, Phys. Rev. Lett. **112**, 047601 (2014).

[14] I. Gross, W. Akhtar, V. Garcia, L. J. Martínez, S. Chouaieb, K. Garcia, C. Carrétéro, A. Barthélémy, P. Appel, P. Maletinsky, J.-V. Kim, J. Y. Chauleau, N. Jaouen, M. Viret, M. Bibes, S. Fusil, and V. Jacques, Real-space imaging of non-collinear antiferromagnetic order with a single-spin magnetometer, Nature (London) **549**, 252 (2017).

[15] L. Thiel, Z. Wang, M. A. Tschudin, D. Rohner, I. Gutiérrez-Lezama, N. Ubrig, M. Gibertini, E. Giannini, A. F. Morpurgo, and P. Maletinsky, Probing magnetism in 2d materials at the nanoscale with single-spin microscopy, Science **364**, 973 (2019).

[16] T. Staudacher, F. Shi, S. Pezzagna, J. Meijer, J. Du, C. A. Meriles, F. Reinhard, and J. Wrachtrup, Nuclear magnetic resonance spectroscopy on a (5-Nanometer)23033 sample volume, Science **339**, 561 (2013).

[17] I. Lovchinsky, A. O. Sushkov, E. Urbach, N. P. de Leon, S. Choi, K. De Greve, R. Evans, R. Gertner, E. Bersin, C. Müller, L. McGuinness, F. Jelezko, R. L. Walsworth, H. Park, and M. D. Lukin, Nuclear magnetic resonance detection and spectroscopy of single proteins using quantum logic, Science **351**, 836 (2016).

[18] R. Schirhagl, K. Chang, M. Loretz, and C. L. Degen, Nitrogen-vacancy centers in diamond: Nanoscale sensors for physics and biology, Annu. Rev. Phys. Chem. **65**, 83 (2014).

[19] D. Le Sage, K. Arai, D. R. Glenn, S. J. DeVience, L. M. Pham, L. Rahn-Lee, M. D. Lukin, A. Yacoby, A. Komeili, and R. L. Walsworth, Optical magnetic imaging of living cells, Nature (London) **496**, 486 (2013).

[20] J. F. Barry, M. J. Turner, J. M. Schloss, D. R. Glenn, Y. Song, M. D. Lukin, H. Park, and R. L. Walsworth, Optical magnetic detection of single-neuron action potentials using quantum defects in diamond, Proc. Natl. Acad. Sci. USA **113**, 14133 (2016).

[21] F. Gorrini, R. Giri, C. E. Avalos, S. Tambalo, S. Mannucci, L. Basso, and N. Bazzanella, Fast and sensitive detection of paramagnetic species using coupled charge and spin dynamics in strongly fluorescent nanodiamonds, ACS Appl. Mater. Interfaces **11**, 24412 (2019).

[22] G. Kucsko, P. C. Maurer, N. Y. Yao, M. Kubo, H. J. Noh, P. K. Lo, H. Park, and M. D. Lukin, Nanometre-scale thermometry in a living cell, Nature (London) **500**, 54 (2013).

[23] M. Fujiwara, S. Sun, A. Dohms, Y. Nishimura, K. Suto, Y. Takezawa, K. Oshimi, Li Zhao, N. Sadzak, Y. Umehara, Y. Teki, N. Komatsu, O. Benson, Y. Shikano, and E. Kage-Nakadai, Real-time nanodiamond thermometry probing in vivo thermogenic responses, Sci. Adv. **6**, eaba9636 (2020).

[24] J. L. Webb, L. Troise, N. W. Hansen, J. Achard, O. Brinza, R. Staacke, M. Kieschnick, J. Meijer, J.-F. Perrier, K. Berg-Sørensen, A. Huck, and U. L. Andersen, Optimization of a diamond nitrogen vacancy centre magnetometer for sensing of biological signals, Front. Phys. **8**, 522536 (2020).

[25] P. Rembold, N. Oshnik, M. M. Müller, S. Montangero, T. Calarco, and E. Neu, Introduction to quantum optimal control

for quantum sensing with nitrogen-vacancy centers in diamond, AVS Quantum Sci. **2**, 024701 (2020).

[26] F. Jelezko and J. Wrachtrup, Single defect centres in diamond: A review, Phys. Status Solidi A **203**, 3207 (2006).

[27] C. Osterkamp, M. Mangold, J. Lang, P. Balasubramanian, T. Teraji, B. Naydenov, and F. Jelezko, Engineering preferentially-aligned nitrogen-vacancy centre ensembles in cvd grown diamond, Sci. Rep. **9**, 5786 (2019).

[28] A. M. Wojciechowski, M. Karadas, C. Osterkamp, S. Jankuhn, J. Meijer, F. Jelezko, A. Huck, and U. L. Andersen, Precision temperature sensing in the presence of magnetic field noise and vice-versa using nitrogen-vacancy centers in diamond, Appl. Phys. Lett. **113**, 013502 (2018).

[29] I. Fescenko, A. Jarmola, I. Savukov, P. Kehayias, J. Smits, J. Damron, N. Ristoff, N. Mosavian, and V. M. Acosta, Diamond magnetometer enhanced by ferrite flux concentrators, Phys. Rev. Research **2**, 023394 (2020).

[30] M. Alkahtani, J. Lang, B. Naydenov, F. Jelezko, and P. Hemmer, Growth of high-purity low-strain fluorescent nanodiamonds, ACS Photonics **6**, 1266 (2019).

[31] A. Dréau, M. Lesik, L. Rondin, P. Spinicelli, O. Arcizet, J. F. Roch, and V. Jacques, Avoiding power broadening in optically detected magnetic resonance of single NV defects for enhanced dc magnetic field sensitivity, Phys. Rev. B **84**, 195204 (2011).

[32] J. F. Barry, J. M. Schloss, E. Bauch, M. J. Turner, C. A. Hart, L. M. Pham, and R. L. Walsworth, Sensitivity Optimization for NV-Diamond Magnetometry, Rev. Mod. Phys. **92**, 015004 (2020).

[33] K. Arai, J. Lee, C. Belthangady, D. R. Glenn, H. Zhang, and R. L. Walsworth, Geometric phase magnetometry using a solid-state spin, Nat. Commun. **9**, 4996 (2018).

[34] T. Nöbauer, A. Angerer, B. Bartels, M. Trupke, S. Rotter, J. Schmiedmayer, F. Mintert, and J. Majer, Smooth Optimal Quantum Control for Robust Solid-State Spin Magnetometry, Phys. Rev. Lett. **115**, 190801 (2015).

[35] T. Wolf, P. Neumann, K. Nakamura, H. Sumiya, T. Ohshima, J. Isoya, and J. Wrachtrup, Subpicotesla Diamond Magnetometry, Phys. Rev. X **5**, 041001 (2015).

[36] D. Suter and F. Jelezko, Single-spin magnetic resonance in the nitrogen-vacancy center of diamond, Prog. Nucl. Magn. Reson. Spectrosc. **98-99**, 50 (2017).

[37] C. Müller, X. Kong, J. M. Cai, K. Melentijevic, A. Stacey, M. Markham, D. Twitchen, J. Isoya, S. Pezzagna, J. Meijer, J. F. Du, M. B. Plenio, B. Naydenov, L. P. McGuinness, and F. Jelezko, Nuclear magnetic resonance spectroscopy with single spin sensitivity, Nat. Commun. **5**, 4703 (2014).

[38] D. Budker, Extreme nuclear magnetic resonance: Zero field, single spins, dark matter, J. Magn. Reson. **306**, 66 (2019).

[39] A. Gruber, A. Dräbenstedt, C. Tietz, L. Fleury, J. Wrachtrup, and C. Von Borczyskowski, Scanning confocal optical microscopy and magnetic resonance on single defect centers, Science **276**, 2012 (1997).

[40] G. Balasubramanian, P. Neumann, D. Twitchen, M. Markham, R. Kolesov, N. Mizuochi, J. Isoya, J. Achard, J. Beck, J. Tissler, V. Jacques, P. R. Hemmer, F. Jelezko, and J. Wrachtrup, Ultralong spin coherence time in isotopically engineered diamond, Nat. Mater. **8**, 383 (2009).

[41] P. Balasubramanian, C. Osterkamp, Y. Chen, X. Chen, T. Teraji, E. Wu, B. Naydenov, and F. Jelezko, dc magnetometry with

engineered nitrogen-vacancy spin ensembles in diamond, Nano Lett. **19**, 6681 (2019).

[42] F. T. Charnock and T. A. Kennedy, Combined optical and microwave approach for performing quantum spin operations on the nitrogen-vacancy center in diamond, Phys. Rev. B **64**, 041201 (2001).

[43] J. M. Schloss, J. F. Barry, M. J. Turner, and R. L. Walsworth, Simultaneous Broadband Vector Magnetometry Using Solid-State Spins, Phys. Rev. Applied **10**, 034044 (2018).

[44] A. Horsley, P. Appel, J. Wolters, J. Achard, A. Tallaire, P. Maletinsky, and P. Treutlein, Microwave Device Characterization Using a Widefield Diamond Microscope, Phys. Rev. Applied **10**, 044039 (2018).

[45] J. Botsoa, T. Sauvage, M.-P. Adam, P. Desgardin, E. Leoni, B. Courtois, F. Treussart, and M.-F. Barthe, Optimal conditions forNV-center formation in type-1b diamond studied using photoluminescence and positron annihilation spectroscopies, Phys. Rev. B **84**, 125209 (2011).

[46] K. M. Itoh and H. Watanabe, Isotope engineering of silicon and diamond for quantum computing and sensing applications, MRS Commun. **4**, 143 (2014).

[47] Y.-I. Sohn, S. Meesala, B. Pingault, H. A. Atikian, J. Holzgrafe, M. Gündoğan, C. Stavrakas, M. J. Stanley, A. Sipahigil, J. Choi, M. Zhang, J. L. Pacheco, J. Abraham, E. Bielejec, M. D. Lukin, M. Atatüre, and M. Lončar, Controlling the coherence of a diamond spin qubit through its strain environment, Nat. Commun. **9**, 2012 (2018).

[48] M. Jamali, I. Gerhardt, M. Rezai, K. Frenner, H. Fedder, and J. Wrachtrup, Microscopic diamond solid-immersion-lenses fabricated around single defect centers by focused ion beam milling, Rev. Sci. Instrum. **85**, 123703 (2014).

[49] S. M. Blakley, C. Vincent, I. V. Fedotov, X. Liu, K. Sower, D. Nodurft, J. Liu, X. Liu, V. N. Agafonov, V. A. Davydov, A. V. Akimov, and A. M. Zheltikov, Photonic-Crystal-Fiber Quantum Probes for High-Resolution Thermal Imaging, Phys. Rev. Applied **13**, 044048 (2020).

[50] R. N. Patel, T. Schröder, N. Wan, L. Li, S. L. Mouradian, E. H. Chen, and D. R. Englund, Efficient photon coupling from a diamond nitrogen vacancy center by integration with silica fiber, Light Sci. Appl. **5**, e16032 (2016).

[51] D. Kim, M. I. Ibrahim, C. Foy, M. E. Trusheim, R. Han, and D. R. Englund, A CMOS-integrated quantum sensor based on nitrogen–vacancy centres, Nat. Electron. **2**, 284 (2019).

[52] J.-M. Cai, B. Naydenov, R. Pfeiffer, L. P. McGuinness, K. D. Jahnke, F. Jelezko, M. B. Plenio, and A. Retzker, Robust dynamical decoupling with concatenated continuous driving, New J. Phys. **14**, 113023 (2012).

[53] G. de Lange, Z. H. Wang, D. Riste, V. V. Dobrovitski, and R. Hanson, Universal dynamical decoupling of a single solid-state spin from a spin bath, Science **330**, 60 (2010).

[54] M. J. Huotari, Biosensing by insect olfactory receptor neurons, Sens. Actuators, B **71**, 212 (2000).

[55] H. A. Kluess, A. J. Stone, and K. W. Evanson, ATP overflow in skeletal muscle 1A arterioles, J. Physiol. **588**, 3089 (2010).

[56] A. de la Escosura-Muñiz and A. Merkoci, Nanochannels Preparation and Application in Biosensing, ACS Nano **6**, 7556 (2012).

[57] B. Bartels and F. Mintert, Smooth optimal control with Floquet theory, Phys. Rev. A **88**, 052315 (2013).

[58] N. Khaneja, T. Reiss, C. Kehlet, T. Schulte-Herbrüggen, and S. J. Glaser, Optimal control of coupled spin dynamics: Design of NMR pulse sequences by gradient ascent algorithms, J. Magn. Reson. **172**, 296 (2005).

[59] R. C. Constantin Brif and H. Rabitz, Control of quantum phenomena: past, present and future, New J. Phys. **12**, 075008 (2010).

[60] B. Bjorn, Smooth Optimal Control of Coherent Quantum Dynamics, PhD. thesis, Albert-Ludwigs-Universitat Freiburg, 2015.

[61] S. Hernández-Gómez, F. Poggiali, P. Cappellaro, and N. Fabbri, Quantum control-enhanced sensing and spectroscopy with NV qubits in diamond, in *Quantum Nanophotonic Materials, Devices, and Systems 2019*, edited by M. Agio, C. Soci, and M. T. Sheldon (SPIE, Bellingham, WA, 2019).

[62] P. Konzelmann, T. Rendler, V. Bergholm, A. Zappe, V. Pfannenstill, M. Garsi, F. Ziem, M. Niethammer, M. Widmann, S. Y. Lee, P. Neumann, and J. Wrachtrup, Robust and efficient quantum optimal control of spin probes in a complex (biological) environment. Towards sensing of fast temperature fluctuations, New J. Phys. **20**, 123013 (2018).

[63] L. Dong, H. Liang, C. K. Duan, Y. Wang, Z. Li, X. Rong, and J. Du, Optimal control of a spin bath, Phys. Rev. A **99**, 013426 (2019).

[64] F. Dolde, V. Bergholm, Ya Wang, I. Jakobi, B. Naydenov, S. Pezzagna, J. Meijer, F. Jelezko, P. Neumann, T. Schulte-Herbrüggen, J. Biamonte, and J. Wrachtrup, High-fidelity spin entanglement using optimal control, Nat. Commun. **5**, 3371 (2014).

[65] J. L. Webb, J. D. Clement, L. Troise, S. Ahmadi, G. J. Johansen, A. Huck, and U. L. Andersen, Nanotesla sensitivity magnetic field sensing using a compact diamond nitrogen-vacancy magnetometer, Appl. Phys. Lett. **114**, 231103 (2019).

[66] F. Poggiali, P. Cappellaro, and N. Fabbri, Optimal Control for One-Qubit Quantum Sensing, Phys. Rev. X **8**, 021059 (2018).

[67] T. E. Skinner, T. O. Reiss, B. Luy, N. Khaneja, and S. J. Glaser, Application of optimal control theory to the design of broadband excitation pulses for high-resolution NMR, J. Magn. Reson. **163**, 8 (2003).

[68] G. Goelman, S. Vega, and D. Zax, Design of broadband propagators in two-level systems, Phys. Rev. A **39**, 5725 (1989).

[69] T. E. Skinner and N. I. Gershenzon, Optimal control design of pulse shapes as analytic functions, J. Magn. Reson. **204**, 248 (2010).

[70] H. A. R. El-Ella, S. Ahmadi, A. M. Wojciechowski, A. Huck, and U. L. Andersen, Optimised frequency modulation for continuous-wave optical magnetic resonance sensing using nitrogen-vacancy ensembles, Opt. Express **25**, 14809 (2017).

[71] See Supplemental Material at http://link.aps.org/supplemental/10.1103/PhysRevB.106.014202 for technical details.

[72] L. Childress, M. V. Gurudev Dutt, J. M. Taylor, A. S. Zibrov, F. Jelezko, J. Wrachtrup, P. R. Hemmer, and M. D. Lukin, Coherent dynamics of coupled electron and nuclear spin qubits in diamond Science **314**, 281 (2006).

[73] S. Ahmadi, Continuous-Wave Magnetic Field Sensing with Nitrogen-Vacancy Centers in Diamond, Ph.D. thesis, Technical University of Denmark, 2018.

[74] A. Genc and R. Baktur, *Tunable Microstrip Bandpass Filters Based on Planar Split Ring Resonators*, IEEE Conference Presentation IEEE, Piscataway, NJ, 2008), p. 4.

[75] E. V. Levine, M. J. Turner, P. Kehayias, C. A. Hart, N. Langellier, R. Trubko, D. R. Glenn, R. R. Fu, and R. L. Walsworth, Principles and techniques of the quantum diamond microscope, Nanophotonics **8**, 1945 (2019).

[76] R. Giri, F. Gorrini, C. Dorigoni, C. E. Avalos, M. Cazzanelli, S. Tambalo, and A. Bifone, Coupled charge and spin dynamics in high-density ensembles of nitrogen-vacancy centers in diamond, Phys. Rev. B **98**, 045401 (2018).

[77] N. B. Manson and J. P. Harrison, Photo-ionization of the nitrogen-vacancy center in diamond, Diam. Relat. Mater. **14**, 1705 (2005).

[78] N. Aslam, G. Waldherr, P. Neumann, F. Jelezko, and J. Wrachtrup, Photo-induced ionization dynamics of the nitrogen vacancy defect in diamond investigated by single-shot charge state detection, New J. Phys. **15**, 013064 (2013).

[79] L. Robledo, H. Bernien, T. van der Sar, and R. Hanson, Spin dynamics in the optical cycle of single nitrogen-vacancy centres in diamond, New J. Phys. **13**, 025013 (2011).

[80] Y. Dumeige, J.-F. Roch, F. Bretenaker, T. Debuisschert, V. Acosta, C. Becher, G. Chatzidrosos, A. Wickenbrock, L. Bougas, A. Wilzewski, and D. Budker, Infrared laser magnetometry with a NV doped diamond intracavity etalon, Opt. Express **27**, 1706 (2019).

[81] F. Ziem, M. Garsi, H. Fedder, and J. Wrachtrup, Quantitative nanoscale MRI with a wide field of view, Sci. Rep. **9**, 12166 (2019).

[82] E. Bauch, C. A. Hart, J. M. Schloss, M. J. Turner, J. F. Barry, P. Kehayias, S. Singh, and R. L. Walsworth, Ultralong Dephasing Times in Solid-State Spin Ensembles via Quantum Control, Phys. Rev. X **8**, 031025 (2018).

[83] L. Busaite, R. Lazda, A. Berzins, M. Auzinsh, R. Ferber, and F. Gahbauer, Dynamic n14 nuclear spin polarization in nitrogen-vacancy centers in diamond, Phys. Rev. B **102**, 224101 (2020).

[84] B. Smeltzer, L. Childress, and A. Gali, 13c hyperfine interactions in the nitrogen-vacancy centre in diamond, New J. Phys. **13**, 025021 (2011).

[85] S. C. Scholten, A. J. Healey, I. O. Robertson, G. J. Abrahams, D. A. Broadway, and J.-P. Tetienne, Widefield quantum microscopy with nitrogen-vacancy centers in diamond: Strengths, limitations, and prospects, J. Appl. Phys. **130**, 150902 (2021).

[86] Y. Nishimura, K. Oshimi, Y. Umehara, Y. Kumon, K. Miyaji, H. Yukawa, Y. Shikano, T. Matsubara, M. Fujiwara, Y. Baba, and Y. Teki, Wide-field fluorescent nanodiamond spin measurements toward real-time large-area intracellular thermometry, Sci. Rep. **11**, 4248 (2021).

[87] A. Gottscholl, M. Kianinia, V. Soltamov, S. Orlinskii, G. Mamin, C. Bradac, C. Kasper, K. Krambrock, A. Sperlich, M. Toth, I. Aharonovich, and V. Dyakonov, Initialization and read-out of intrinsic spin defects in a van der Waals crystal at room temperature, Nat. Mater. **19**, 540 (2020).